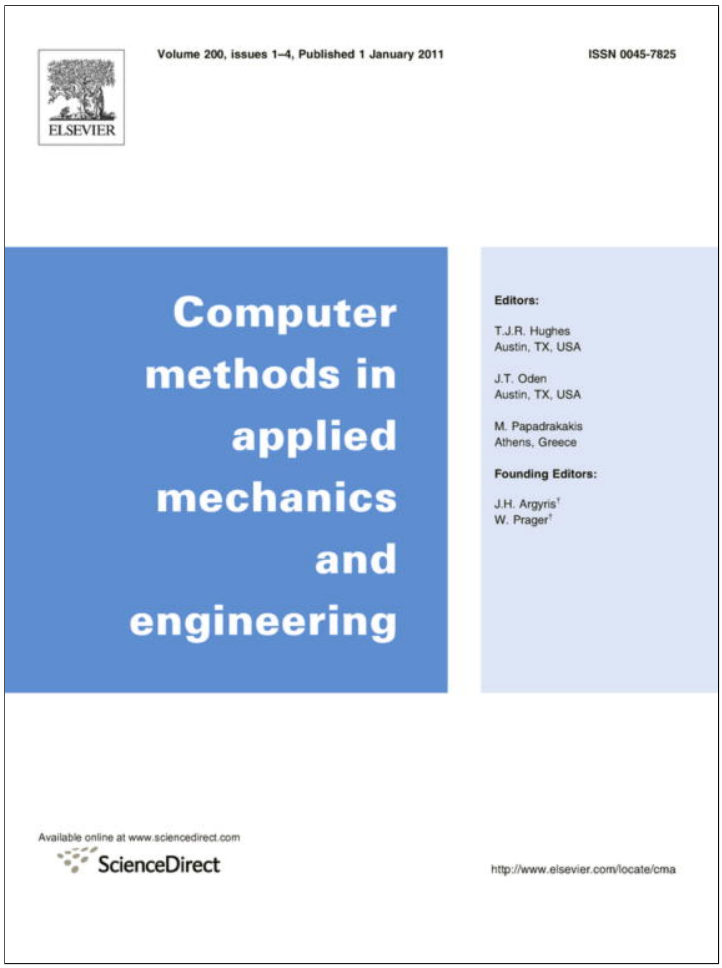

(This is a sample cover image for this issue. The actual cover is not yet available at this time.)

Comput. Methods Appl. Mech. Engrg. 200 (2011) 3482–3494

Contents lists available at SciVerse ScienceDirect

Comput. Methods Appl. Mech. Engrg.

journal homepage: www.elsevier.com/locate/cma

Coupling of finite element method with material point method by local multi-mesh contact method ☆

Y.P. Lian, X. Zhang *, Y. Liu

AML, School of Aerospace, Tsinghua University, Beijing 100084, PR China

ARTICLE INFO

Article history:
Received 21 March 2011
Received in revised form 5 July 2011
Accepted 28 July 2011
Available online 5 August 2011

Keywords:
Material point method
Finite element method
Extreme deformation
Contact

ABSTRACT

As a Lagrangian particle method, the material point method (MPM) has the potential to model extreme deformation of materials, where the traditional finite element method (FEM) often encounters mesh distortion and element entanglement which lead to numerical difficulties. However, FEM is more accurate and efficient than MPM for problems with small deformation. It is therefore desirable to model the body with extreme deformation by MPM and the body with small deformation by FEM, respectively. In this paper, a method to handle the contact interaction between the MPM body and the FEM body is proposed, which is implemented on the background grid of MPM. By this method, FEM is coupled with MPM and a hexahedral element is incorporated into our 3D explicit MPM code MPM3D®. Several numerical examples, including plate impact, sphere rolling, perforation of thick plate, and fluid–structure interaction problems, are studied and the numerical results are in good agreement with analytical solution and results available in the literature. The coupling of FEM and MPM offers advantages of both FEM and MPM.

1. Introduction

In recent decades, many Lagrangian meshless/meshfree and particle methods have been proposed to solve challenging mechanics problems, such as hyper-velocity impact, explosion, dynamic crack propagation, fluid–structure interaction (FSI) problems and so on. The smoothed particle hydrodynamics (SPH) method was proposed and used early for hyper-velocity impact [1–3]. Johnson et al. [4,5] have done a lot of work to improve and apply SPH for impact and penetration problems; Rabczuk and Eibl [6] applied improved SPH–MLSPH to model dynamic failure of concrete; Liu et al. [7,8] applied SPH for explosion problems. For the crack problem, Belytschko and Tabbara [9] applied the element-free Galerkin method (EFGM) for the dynamic crack propagation for the first time. Then Rabczuk and Belytschko [10,11] developed a cracking particles method based on step function, namely EFG-P, which used cracked particle to represent the crack surface and to model the fracture of concrete. Similarly, Rabczuk and Zi [12], Rabczuk et al. [13] put forward an extended element free Galerkin method, XEFGM. For the FSI problem, Idelsohn et al. [14] proposed a particle finite element method (PFEM) for solving incompressible flows with free-surfaces and breaking waves. Recently, Rabczuk et al. [15] put forward an immersed particle method for FSI of fracturing structures under high pressure loads, where both the structure and fluid are treated by meshfree method. Another representative of such methods is the material point method (MPM) [16], which has been used for impact [17,18] and penetration [19,20], explosion [21,22], dynamic crack propagation [23,24], film delamination [25], FSI [26,27] and saturated soil-structure interaction problems [28], just to name a few.

Up to now, many techniques have appeared for the coupling of meshless/meshfree methods with FEM. Rabczuk et al. [29] gave a detailed review of the various methods for coupling, such as master–slave coupling [4,30,31], coupling via mixed interpolation [32], coupling with Lagrange multipliers [33,34], and so on.

Attaway et al. [35] coupled SPH with FEM through master–slave algorithm for the first time. Using this coupled method, in each time step, they detected whether slave particles penetrate master element faces. Following the contact detection, a contact constraint is applied to calculate forces that push the slave particles back to remain on the master surface. Similarly, Johnson et al. [31,4] coupled SPH and FEM by master–slave algorithm with application for high velocity impact problems. Then Johnson and Stryk [36] extended this coupled particle method by converting damaged or failure elements into particles. Afterwards, Rabzuk et al. proposed an alternative method where the particles are rigidly fixed to the FE nodes via master–slave coupling [29]. Recently, Vuyst et al. [37] presented a novel method of combining SPH and FEM with contact method of SPH by treating the nodes as meshless particles.

Besides SPH, Belytschko et al. [32] developed a coupled method for EFGM and FEM. Interface elements between EFGM and FEM

☆ Supported by National Basic Research Program of China (2010CB832701) and National Natural Science Foundation of China (10872107).
* Corresponding author.
E-mail address: xzhang@tsinghua.edu.cn (X. Zhang).

0045-7825/$ - see front matter © 2011 Elsevier B.V. All rights reserved.
doi:10.1016/j.cma.2011.07.014

domains is employed with the shape function composed of FEM and EFGM shape functions. In addition, Hegen [33] coupled FEM with EFGM via Lagrange multipliers. Furthermore, Rabczuk and Belytschko [34] extended this coupled scheme to non-linear problems and applied it to deformable interfaces. For other meshless methods, Liu et al. [38] coupled the reproducing kernel particle method (RKPM) with FEM by modifying the shape functions in the transition area for both RKPM and FEM. Besides this, Liu and Li et al. [39–41] proposed a new method called reproducing kernel element method (RKEM) to combine the advantages of both FEM and meshless methods.

For MPM, Zhang et al. [19] developed a coupling method called explicit material point finite element (MPFE) method. In this method, the material domain is discretized initially by a mesh of finite elements with a predefined computational grid in the potential large deformation region. The nodes located in the predefined grid are treated as particles and their momentum equations are solved on the grid, whereas the remaining nodes are treated as finite element (FE) nodes whose momentum equations are solved on the FE mesh. Further, Zhang et al. proposed a FEMP method [20] for modeling reinforced concrete subjected to impact loading. The essential idea of this method is to introduce a hybrid bar element into MPM, where the nodal variables are updated from background grid and the stresses are updated on the element. By this hybrid bar element, the reinforced bar in concrete can be discretized easily.

In MPM, material domain is discretized with a set of Lagrangian material points (particles), which carry all state variables in order to model history-dependent materials. An Eulerian background grid is used to integrate the momentum equation. In each time step, the particles are rigidly attached to background grid and move with the grid. Then Kinematic variables are first mapped from particles to grid points to establish the momentum equations on background grid. Afterwards, the solutions of the momentum equation are mapped from grid points back to particles to update their positions and velocities. At the end of each time step, the deformed grid is discarded and a new regular grid is defined for the next time step. Hence, mesh distortion and element entanglement associated with the FEM are overcome; while numerical dissipation normally associated with Eulerian method is avoided.

Although MPM can be more accurate, more efficient and more robust than FEM for problems involving severe distortions, the accuracy of particle quadrature used in MPM is lower than that of Gauss quadrature used in FEM. As a result, it is less accurate and efficient than FEM for problems with small deformation. In addition, MPM requires more computational storage because it makes use of both grid and particle data. Moreover, FEM is with more mature development and comprehensive capabilities. In this paper, to take advantages of both methods, FEM is coupled with MPM, in which the body with mild deformation is modeled by FEM, while the body with extreme deformation is modeled by MPM. The interaction between the FEM body and the MPM body is handled by a local multi-mesh contact method [42–44,47]. The FE nodes located on the contact interface are treated as particles, so that the contact force is calculated on the background grid point to avoid penetration between the FEM body and the MPM body. Furthermore, a Coulomb friction model is implemented to allow friction slipping between bodies. This coupled finite element–material point (CFEMP) method is implemented in our 3D explicit MPM code MPM3D® and several numerical examples are studied to validate the CFEMP method. Numerical results are in good agreement with analytical and available results.

The remaining parts of the paper are organized as follows. A brief review of the MPM and the FEM solution schemes is presented in Section 2, while the contact method for coupling MPM with FEM is presented in detail in Section 3. The numerical implementation of the proposed method is summarized in Section 4, and several numerical examples mentioned above are presented in Section 5. Finally, conclusions are given in Section 6.

2. Brief review of MPM and FEM solution schemes

2.1. Governing equations

In material domain Ω, the basic equations of continuum mechanics in an updated Lagrangian description are the mass conservation

$$\rho(\boldsymbol{X},t)J(\boldsymbol{X},t)=\rho_0(\boldsymbol{X}), \tag{1}$$

the momentum conservation

$$\sigma_{ij,j}+\rho f_i=\rho\ddot{u}_i \tag{2}$$

and the energy equation

$$\rho\dot{w}^{\text{int}}=D_{ij}\sigma_{ij}, \tag{3}$$

with the boundary conditions

$$\begin{cases}(n_j\sigma_{ij})|_{\Gamma_t}=\bar{t}_i,\\ u_i|_{\Gamma_v}=\bar{u}_i\end{cases} \tag{4}$$

and initial conditions

$$\begin{cases}\dot{u}(\boldsymbol{X},0)=\dot{u}_0(\boldsymbol{X}),\\ u(\boldsymbol{X},0)=u_0(\boldsymbol{X}).\end{cases} \tag{5}$$

In the above equations, subscripts i and j denote the component of the space with Einstein summation convention, subscript 0 signifies the initial value, the comma denotes covariant differentiation, and the superimposed dot indicates the time derivatives. ρ is the current density, J is the Jacobian determinant, $\boldsymbol{X}$ is the Lagrangian coordinate, σ_{ij} is the Cauchy stress, f_i is the body force per unit mass, u_i is the displacement, D_{ij} is the rate-of-deformation, w is the internal energy per unit mass, and n_j is the unit outward normal to the boundary. Γ_t and Γ_u signify the prescribed traction boundary and displacement boundary of Ω, respectively.

Taking the virtual displacement δu_i as test function, the weak form of the momentum equation can be obtained by the weighted residual method as

$$\int_\Omega\rho\ddot{u}_i\delta u_i\mathrm{d}\Omega+\int_\Omega\sigma_{ij}\delta u_{i,j}\mathrm{d}\Omega-\int_\Omega\rho f_i\delta u_i\mathrm{d}\Omega-\int_{\Gamma_t}\bar{t}_i\delta u_i\mathrm{d}\Gamma=0, \tag{6}$$

where the displacement boundary conditions are assumed to be satisfied as a *priori*.

2.2. MPM solution scheme

In MPM, the material domain is discretized by a set of particles, as shown in Fig. 1. As a result, the mass is lumped at each particle so that the density is approximated by

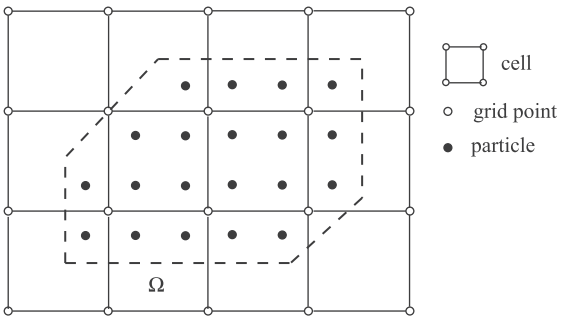

Fig. 1. MPM discretization sketch.

$$\rho(\boldsymbol{x}) = \sum_{p=1}^{n_p} m_p \delta(\boldsymbol{x} - \boldsymbol{x}_p), \tag{7}$$

where n_p is the total number of the particles, m_p is the mass of particle p, $\boldsymbol{x}_p$ is the coordinate of particle p, and δ is the Dirac delta function.

As particles are rigidly attached to the background grid in each time step, the kinematic information can be mapped between particles and grid points through the shape functions of the grid cell. For example, the grid nodal momentum can be obtained by mapping the particles momenta to the grid point, namely,

$$P_{iI} = \sum_{p=1}^{n_p} N_{Ip} m_p v_{ip}, \tag{8}$$

where subscripts p and I denote variables associated with particle p and grid point I, respectively. $N_{Ip} = N_I(\boldsymbol{x}_p)$ is the value of shape function of grid point I evaluated at the site of particle p. In this paper, the 8-point hexahedral cell is employed, so that

$$N_{Ip} = \frac{1}{8}(1+\xi\xi_I)(1+\eta\eta_I)(1+\zeta\zeta_I) \quad I = 1,2,\ldots,8, \tag{9}$$

where ($\xi \in [-1,1]$, $\eta \in [-1,1]$, $\zeta \in [-1,1]$) are the nature coordinates of particle p, ξ_I, η_I and ζ_I take on their nodal value of (±1,±1,±1). If the particle p is outside of the cell, N_{Ip} is equal to zero.

Substituting Eqs. (7) and (8) into Eq. (6) and invoking the arbitrariness of δu_{iI} lead to

$$\dot{p}_{iI} = f_{iI} \quad I = 1,2,\ldots,n_g, \tag{10}$$

where

$$p_{iI} = m_I v_{iI} \tag{11}$$

is the momentum of grid point I,

$$f_{iI} = f_{iI}^{\text{ext}} + f_{iI}^{\text{int}} \tag{12}$$

is the nodal force of grid point I,

$$f_{iI}^{\text{int}} = -\sum_{p=1}^{n_p} N_{Ip,j}\sigma_{ijp}\frac{m_p}{\rho_p} \tag{13}$$

is the internal force,

$$f_{iI}^{\text{ext}} = \sum_{p=1}^{n_p} N_{Ip}\bar{t}_{ip}h^{-1}\frac{m_p}{\rho_p} + \sum_{p=1}^{n_p} m_p N_{Ip} f_{ip} \tag{14}$$

is the external force, $\sigma_{ijp} = \sigma_{ij}(\boldsymbol{x}_p)$, $f_{ip} = f_i(\boldsymbol{x}_p)$, $\bar{t}_{ip} = \bar{t}_i(\boldsymbol{x}_p)$, and h denotes the thickness of the layer of the boundary. In Eq. (11), the lumped mass matrix is used, namely

$$m_I = \sum_{p=1}^{n_p} m_p N_{Ip}. \tag{15}$$

2.3. FEM solution scheme

In FEM, the weak form of Eq. (6) can be used directly without any modifications. In this paper, the 8-node hexahedron element is implemented and the shape functions are the same to that given in Eq. (9). Consequently, the displacement u_i of material point $\boldsymbol{X}$ can be approximated by

$$u_i(\boldsymbol{X},t) = \sum_{K=1}^{8} N_K(\xi(\boldsymbol{X}))u_{iK}(t), \tag{16}$$

where the subscript K denotes the FE nodes. The integration over material domain in Eq. (6) can be calculated as the summation of the integration over all elements. Substituting Eq. (16) into Eq. (6) yields

$$\dot{p}_{iK} = f_{iK}, \tag{17}$$

where

$$p_{iK} = m_K v_{iK} \tag{18}$$

is the momentum of FE node K,

$$f_{iK} = f_{iK}^{\text{int}} + f_{iK}^{\text{ext}} + f_{iK}^{\Gamma} \tag{19}$$

is the nodal force of FE node K,

$$f_{iK}^{\text{int}} = -\sum_e \int_{V_e} N_{K,j}\sigma_{ji}dV = -\sum_e N_{Ke,j}\sigma_{jie}V_e \tag{20}$$

is the internal force of FE node K,

$$f_{iK}^{\text{ext}} = \sum_e \left(\int_{V_e} \rho N_K f_i dV + \int_{\Gamma_{te}} N_K \bar{t}_i d\Gamma\right) = \sum_e \left(m_e N_{Ke} f_{ie} + \int_{\Gamma_{te}} N_K \bar{t}_i d\Gamma\right) \tag{21}$$

is the external force, and f_{iK}^{Γ} is the hourglass-resisting nodal force to control the hourglass modes caused by one-point Gauss quadrature. Both the standard and Flanagan–Belytschko hourglass control schemes [45,46] are implemented in CFEMP method.

In Eqs. (20) and (21), subscript e denotes the value at the center of element e, and $m_e = \rho_e V_e$.

3. Coupling scheme

From Section 2, it can be found that MPM is very similar to FEM in one time step, so that FEM can be coupled with MPM readily by the contact method. A coupling scheme is developed based on the local multi-mesh contact method [47] in the framework of MPM. In each time step, MPM bodies and FEM bodies are first updated independently to obtain their trial values of nodal variables, as if they were not in contact. If the momenta of a MPM body and a FEM body are projected to the same grid point, two bodies contact at the grid point, so a contact force is imposed on them to prevent penetration.

In order to describe the algorithm more clearly, two bodies, as shown in Fig. 2, are considered. Body r, denoted by Ω_F, is modeled by FEM, while body s, denoted by Ω_M, is modeled by MPM. If contact occurs at a grid point I, the FE node which is located on the surface of body r and has contribution to the grid point I is termed as hybrid node. Nodes a, b, and c in Fig. 2 are typical hybrid nodes.

3.1. Time integration

The central difference time integration algorithm is used to integrate the momentum equation, as shown in Fig. 3, where $t^{k+1} = t^k + \Delta t^{k+1/2}$, $t^{k+1/2} = t^k + \Delta t^{k+1/2}/2 = t^{k-1/2} + \Delta t^k$ and $\Delta t^k = (\Delta t^{k-1/2} + \Delta t^{k+1/2})/2$.

In the follows, the superscript k denotes the value of variable at time t^k. Given u_{ip}^k and $\dot{u}_{ip}^{k-1/2}$, we seek for the solution at time t^{k+1}.

3.1.1. Time integration in domain Ω_M

From Eq. (10), the momentum of grid point at time $t^{k+1/2}$ can be updated by

$$p_{iI}^{k+1/2} = p_{iI}^{k-1/2} + f_{iI}^k \Delta t^k, \tag{22}$$

where f_{iI}^k is the nodal force of grid point I at time t^k given in Eq. (12).

The velocities and the positions of particles at time $t^{k+1/2}$ and t^{k+1}, respectively, are updated by

$$v_{ip}^{k+1/2} = v_{ip}^{k-1/2} + \Delta t^k \sum_{I=1}^{n_g} f_{iI}^k N_{Ip}^k / m_I^k, \tag{23}$$

$$x_{ip}^{k+1} = x_{ip}^k + \Delta t^{k+1/2} \sum_{I=1}^{n_g} p_{iI}^{k+1/2} N_{Ip}^k / m_I^k. \tag{24}$$

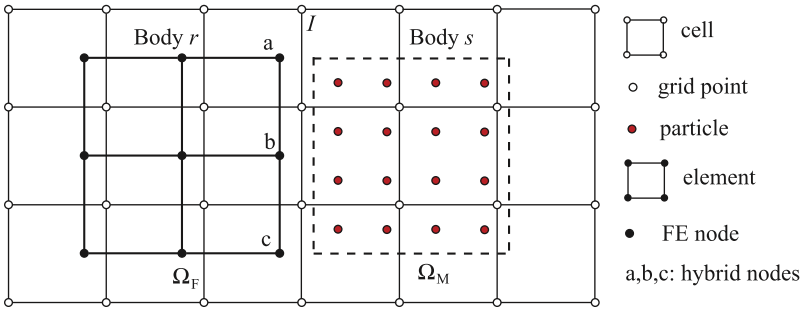

Fig. 2. 2D illustration of coupling FEM with MPM.

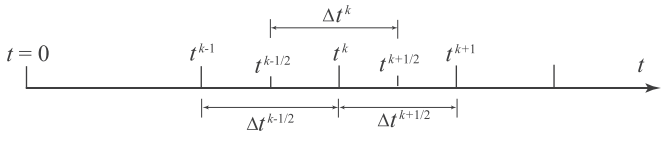

Fig. 3. Time integration.

3.1.2. Time integration in domain Ω_F

For the hybrid nodes, the velocities at time $t^{k+1/2}$ are updated in a way similar to the particles from the background grid as

$$v_{iK}^{k+1/2} = v_{iK}^{k-1/2} + \Delta t^k \sum_{I=1}^{n_g} f_{iI}^k N_{IK}^k / m_I^k + f_{iK}^{k,\Gamma} \Delta t^k / m_J, \tag{25}$$

where the subscript I denotes the point of the background grid, f_{iI}^k is the nodal force of grid point I at time t^k, and f_{iK}^{Γ} is the hourglass resisting force.

For other FE nodes, the velocities at time $t^{k+1/2}$ are updated from Eq. (17) as

$$v_{iK}^{k+1/2} = v_{iK}^{k-1/2} + f_{iK}^k \Delta t^k / m_J. \tag{26}$$

The nodal positions at time t^{k+1} are updated by

$$x_{iK}^{k+1} = x_{iK}^k + v_{iK}^{k+1/2} \Delta t^{k+1/2}. \tag{27}$$

3.1.3. Critical time step

Both MPM and FEM use the central difference time integration algorithm so that the critical time step size is determined by

$$\Delta t = \min(L_e / c), \tag{28}$$

where L_e is the characteristic length of cell e in MPM and element e in FEM, and c is the material local sound speed. The characteristic length L_e in MPM is constant due to the regular background grid cell used. In contrast, the characteristic length L_e in FEM is variable due to the deformation of the element. In order to keep all operations synchronic in the same loop, the minimum critical time step size of FEM and MPM domains is used as the time step size. Therefore, the L_e of FEM should not be less than that of MPM so that the critical time step is dependent on the MPM domain.

3.1.4. Artificial bulk viscosity

In order to treat shock waves, artificial bulk viscosity q [45] is applied, which is defined as:

$$q = \begin{cases} c_0 \rho L_e^2 (\dot{\varepsilon}_{kk})^2 - c_1 \rho L_e c \dot{\varepsilon}_{kk} & \text{if} \quad \dot{\varepsilon}_{kk} < 0, \\ 0 & \text{if} \quad \dot{\varepsilon}_{kk} \geqslant 0, \end{cases} \tag{29}$$

where c_0 and c_1 are dimensionless constants, c is the local sound speed, $\dot{\varepsilon}_{kk}$ is the trace of the strain rate tensor. L_e is the characteristic length of grid cell in MPM, and the characteristic length of element in FEM.

3.2. Contact detection

The contact detection is accomplished by monitoring the interaction of different velocity fields at the same grid point. The masses and the momenta of the particles of MPM body s and the nodes located on the surface of FEM body r are mapped to the background grid. Then the velocity of grid point I contributed from body b can be obtained as

$$v_{iI}^{b,k-1/2} = \frac{p_{iI}^{b,k-1/2}}{m_I^{b,k}}, \tag{30}$$

where the superscript b denotes the value mapped from body b, $m_I^{b,k}$ and $p_{iI}^{b,k-1/2}$ are the mass and the momentum of grid point I, respectively. If the momenta of two bodies are mapped to the same grid point, the contact may occur. That is to say, when

$$(v_{iI}^{r,k-1/2} - v_{iI}^{s,k-1/2}) n_{iI}^{r,k} > 0 \tag{31}$$

is satisfied, the FEM body contacts with the MPM body in the vicinity of grid point I. In Eq. (31), $n_{iI}^{r,k}$ is the unit outward normal of body r at point I along the boundary. In the FEM domain Ω_F, $n_{iI}^{r,k}$ equals to the summation of normal vectors of the element faces in which the hybrid nodes with contributions to the grid point are located. The direction of gradient of mass of a body with constant density along the boundary is outward normal to the boundary. Hence, the gradient of mass evaluated at the grid point of the computational grid provides an approximation for the normal direction at the surface of the body. In the MPM domain Ω_M, where the mass is lumped at each particle, $n_{iI}^{s,k}$ can be calculated approximately by the gradient of the mass [42] as

$$n_{iI}^{s,k} = \sum_p N_{Ip,i}^k m_p. \tag{32}$$

Multiplied by $m_I^{r,k} m_I^{s,k}$, Eq. (31) can be rewritten as

$$\left(m_I^{s,k} p_{iI}^{r,k-1/2} - m_I^{r,k} p_{iI}^{s,k-1/2} \right) n_{iI}^{r,k} > 0. \tag{33}$$

When using the contact detection condition Eq. (33), two bodies may contact if the space between them is less than two times the grid cell size, which makes contact occur earlier than the actual contact time. The improved contact detection method proposed by Ma et al. [47] is used here to prevent the earlier contact.

3.3. Contact force

If two bodies contact at grid point I, contact forces must be imposed on them to prevent penetration. After imposing the contact force $f_{iI}^{b,c,k}$, the updated momentum p_{iI}^b of body b is given by

$$p_{iI}^{b,k+1/2} = \bar{p}_{iI}^{b,k+1/2} + \Delta t^k f_{iI}^{b,c,k}, \tag{34}$$

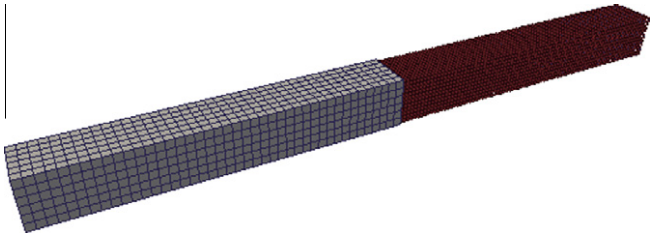

Fig. 4. Typical discretization of plate impact.

where

$$\bar{p}_{il}^{b,k+1/2} = p_{il}^{b,k-1/2} + \Delta t^k f_{il}^{b,k} \tag{35}$$

is the trial value of the grid nodal momentum, $p_{il}^{b,k-1/2}$ is the grid nodal momentum at the beginning of each time step, and $f_{il}^{b,c,k}$ is the contact force applied on body b at time step t^k.

The updated momentum must satisfy the impenetrability condition

$$\left(m_I^{s,k} p_{il}^{r,k+1/2} - m_I^{r,k} p_{il}^{s,k+1/2}\right) n_{il}^{r,k} = 0. \tag{36}$$

By substituting Eq. (34) into Eq. (36), the normal contact force $f_I^{\mathrm{nor},k} = f_{il}^{r,c,k} n_{il}^{r,k} = -f_{il}^{s,c,k} n_{il}^{r,k}$ can be obtained as

$$f_I^{\mathrm{nor},k} = \frac{\left(m_I^{s,k} \bar{p}_{il}^{r,k+1/2} - m_I^{r,k} \bar{p}_{il}^{s,k+1/2}\right) n_{il}^{r,k}}{\left(m_I^{r,k} + m_I^{s,k}\right)\Delta t} = f_{I,1}^{\mathrm{nor},k} + f_{I,2}^{\mathrm{nor},k}, \tag{37}$$

where

$$f_{I,1}^{\mathrm{nor},k} = \frac{\left(m_I^{s,k} p_{il}^{r,k-1/2} - m_I^{r,k} p_{il}^{s,k-1/2}\right) n_{il}^{r,k}}{\left(m_I^{r,k} + m_I^{s,k}\right)\Delta t}, \tag{38}$$

$$f_{I,2}^{\mathrm{nor},k} = \frac{\left(m_I^{s,k} f_{il}^{r,k} - m_I^{r,k} f_{il}^{s,k}\right) n_{il}^{r,k}}{\left(m_I^{r,k} + m_I^{s,k}\right)}. \tag{39}$$

In the above, $f_{il}^{s,k}$ is the nodal force of grid point I contributed from MPM body s by Eq. (12), and $f_{il}^{r,k}$ is the nodal force of grid point I contributed from FEM body r by

$$f_{il}^{r,k} = \sum_{J=1}^{n_h} N_{IK} f_{iK}^{r,k}, \tag{40}$$

where n_h is the total number of the hybrid node, and $f_{iK}^{r,k}$ is the nodal force of hybrid node K given by Eq. (19).

For stick contact, substituting Eq. (34) into the non-slip condition

$$\left(m_I^{s,k} p_{il}^{r,k+1/2} - m_I^{r,k} p_{il}^{s,k+1/2}\right) t_{il}^{r,k} = 0, \tag{41}$$

the tangential contact force $f_I^{\mathrm{stick},k} = f_{il}^{r,c,k} t_{il}^{r,k} = -f_{il}^{s,c,k} t_{il}^{r,k}$ can be obtained as

$$f_I^{\mathrm{stick},k} = \frac{\left(m_I^{s,k} \bar{p}_{il}^{r,k+1/2} - m_I^{r,k} \bar{p}_{il}^{s,k+1/2}\right) t_{il}^{r,k}}{\left(m_I^{r,k} + m_I^{s,k}\right)\Delta t} = \frac{\left(m_I^{s,k} p_{il}^{r,k-1/2} - m_I^{r,k} p_{il}^{s,k-1/2}\right) t_{il}^{r,k}}{\left(m_I^{r,k} + m_I^{s,k}\right)\Delta t} + \frac{\left(m_I^{s,k} f_{il}^{r,k} - m_I^{r,k} f_{il}^{s,k}\right) t_{il}^{r,k}}{\left(m_I^{r,k} + m_I^{s,k}\right)}. \tag{42}$$

In Eq. (41), $t_{il}^{r,k}$ is the unit tangent at grid point I along the boundary, which can be determined by

$$t_{il}^{r,k} = \frac{\left(v_{il}^{r,k-1/2} - v_{il}^{s,k-1/2}\right) - \left(v_{jl}^{r,k-1/2} - v_{jl}^{s,k-1/2}\right) n_{jl}^{r,k} n_{il}^{r,k}}{\left|\left(v_{il}^{r,k-1/2} - v_{il}^{s,k-1/2}\right) - \left(v_{jl}^{r,k-1/2} - v_{jl}^{s,k-1/2}\right) n_{jl}^{r,k} n_{il}^{r,k}\right|}. \tag{43}$$

For slip contact, the friction at the contact surface is described by the Coulomb friction model, in which the friction force is limited to $\mu f_I^{\mathrm{nor},k}$, where μ is the friction coefficient. Therefore, the tangential contact force can be obtained as

$$f_I^{\tan,k} = \min\left(\mu f_I^{\mathrm{nor},k}, f_I^{\mathrm{stick},k}\right). \tag{44}$$

Finally, the contact force applied on body b can be expressed as

$$f_{il}^{b,c,k} = f_I^{\mathrm{nor},k} n_{il}^{b,k} + f_I^{\tan,k} t_{il}^{b,k}. \tag{45}$$

3.4. Stress update

In CFEMP, the stress at the time $t^{k+1/2}$ is updated by

$$\sigma_{ij}^{k+1} = \sigma_{ij}^{k} + \dot{\sigma}_{ij}^{k-1/2} \Delta t^{k+1/2}, \tag{46}$$

where $\dot{\sigma}_{ij}$ is the material time derivative of the stress. $\dot{\sigma}_{ij}$ is determined by

$$\dot{\sigma}_{ij} = \sigma_{ij}^{\nabla} + \sigma_{ik}\Omega_{jk} + \sigma_{jk}\Omega_{ik}, \tag{47}$$

where σ_{ij}^{∇} is the Jaumann (co-rotational) stress rate, and Ω_{ij} is the spin tensor. σ_{ij}^{∇} is determined from the strain rate $\dot{\varepsilon}_{ij}$ by a constitutive model.

In domain Ω_{F}, the strain rate and spin tensor are calculated at the element center by

$$\dot{\varepsilon}_{ije} = \frac{1}{2}\sum_{I=1}^{8}\left(N_{Ie,j}\dot{u}_{iI} + N_{Ie,i}\dot{u}_{jI}\right), \tag{48}$$

$$\Omega_{ije} = \frac{1}{2}\sum_{I=1}^{8}\left(N_{Ie,j}\dot{u}_{iI} - N_{Ie,i}\dot{u}_{jI}\right). \tag{49}$$

In domain Ω_{M}, the strain rate and spin tensor are calculated at the particle by

$$\dot{\varepsilon}_{ijp} = \frac{1}{2}\sum_{I=1}^{8}\left(N_{Ip,j}\dot{u}_{iI} + N_{Ip,i}\dot{u}_{jI}\right), \tag{50}$$

$$\Omega_{ijp} = \frac{1}{2}\sum_{I=1}^{8}\left(N_{Ip,j}\dot{u}_{iI} - N_{Ip,i}\dot{u}_{jI}\right). \tag{51}$$

The deviatoric stress and the pressure are updated here with a constitutive law and an equation of state (EOS), respectively.

4. Numerical implementation

It should be noted that $f_{I,1}^{\mathrm{nor},k}$, the first part of the normal contact force in Eq. (37), will vanish if the momenta $p_{il}^{b,k-1/2}$ at the beginning of each time step satisfy the impenetrability condition Eq. (36). However, the deformed background grid in MPM is discarded at the end of each time step, and a new regular background grid is redefined for the next time step. Therefore, the impenetrability condition (36) may not be satisfied at the beginning of each time step, even if it has been imposed at the end of last time step [43]. As pointed out by Huang et al. [43], the nodal velocities $v_{il}^{b,k-1/2}$ used to update the stresses may violate the impenetrability condition Eq. (36), which may introduce disturbance to the system.

To eliminate the artificial disturbance, before updating stresses of particles, the nodal momenta $p_{il}^{s,k-1/2}$ of grid point I are adjusted to their new values $\tilde{p}_{il}^{s,k-1/2}$ by using

$$\tilde{p}_{il}^{s,k-1/2} = p_{il}^{s,k-1/2} + \Delta t^k f_{I,1}^{\mathrm{nor},k} n_{il}^{s,k}, \tag{52}$$

where $f_{I,1}^{\mathrm{nor},k}$ is defined in Eq. (38). It can be verified that the adjusted nodal momenta $\tilde{p}_{il}^{s,k-1/2}$ satisfy the impenetrability condition Eq. (36). The velocities of hybrid nodes in FEM body r are also adjusted for the reason same to above by using

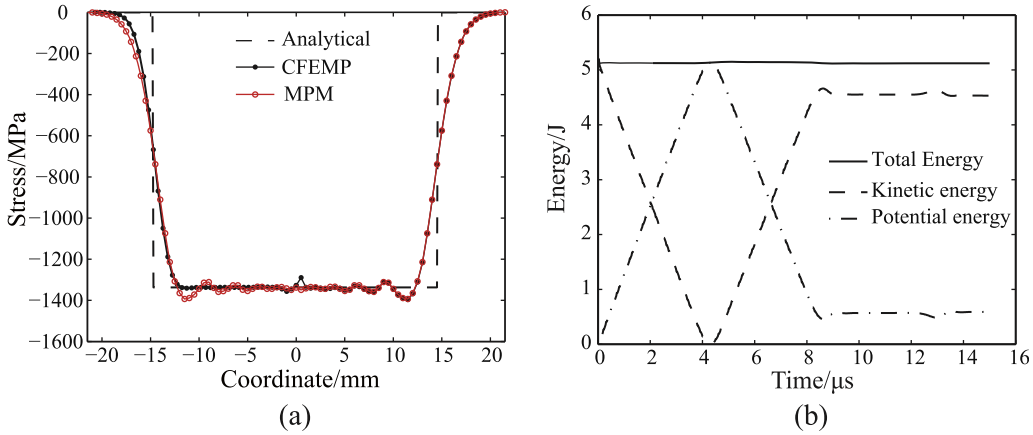

Fig. 5. (a) Plate impact stress profile at time 3.0 μs; (b) Energy evolution of plate impact.

$$\tilde{v}_{iK}^{r,k-1/2} = v_{iK}^{r,k-1/2} + \Delta t^k \sum_{I=1}^{n_g} f_{I,1}^{\mathrm{nor},k} n_{iI}^{r,k} N_{IK}^k / m_I^{r,k}. \tag{53}$$

The detailed implementation of the method is presented as follows.

1. Initialize background grid points.
   Loop over all the particles in MPM body s to calculate their contributions to the masses and the momenta of grid points by
   $$m_I^{s,k} = \sum_p m_p^s N_{Ip}^k, \tag{54}$$
   $$p_{iI}^{s,k-1/2} = \sum_p m_p^s v_{ip}^{s,k-1/2} N_{Ip}^k. \tag{55}$$
   Loop over all the FE nodes located at the surface of FEM body r to calculate their contributions to the masses $m_I^{r,k}$ and momenta $p_{iI}^{r,k-1/2}$ of grid points in a way similar to that in Eqs. (54) and (55).
2. Apply the boundary conditions.
3. Detect the contact grid points.
   Loop over all the grid points to detect the contact grid points. If Eq. (33) is satisfied and the real physical distance between two bodies is less than a prescribed value, the two bodies contact at the grid point I. Label FE nodes which have contributions to the grid point I as hybrid nodes.
4. Loop over all the contact grid points to adjust their momenta $p_{iI}^{s,k-1/2}$ to new values $\tilde{p}_{iI}^{s,k-1/2}$ according to Eq. (52). Then loop over all the hybrid nodes to adjust their velocities $v_{iI}^{r,k-1/2}$ to new values $\tilde{v}_{iI}^{r,k-1/2}$ according to Eq. (53).
5. Update stresses.
   Loop over all the particles to calculate their incremental strains and spin tensors, respectively, from the background grid by using

Table 1
Information for plate impact.

	Elements	Particles	Time steps to 15 μs	Cost/s	Separation time/μs
Analytical	–	–	–	–	8.63
CFEMP	1512	12,096	695	50	8.7
MPM	–	24,192	695	97	8.7

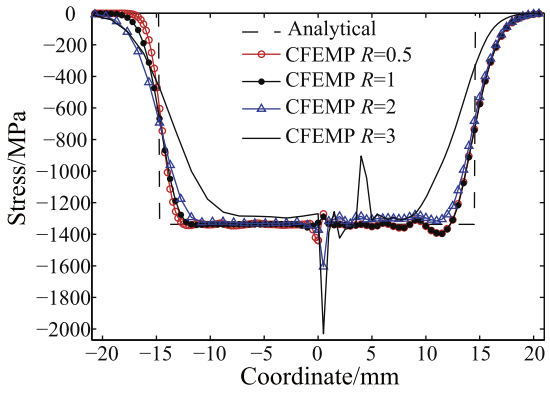

Fig. 6. Plate impact stress profile at time 3.0 μs for different ratio by fixing cell size 0.5 mm.

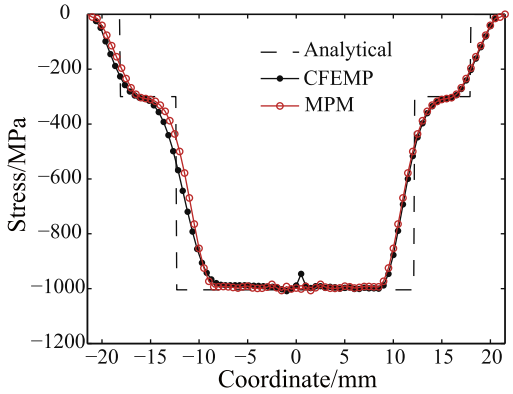

Fig. 7. Plate impact stress profile at time 3.7 μs.

$$\Delta\varepsilon_{ijp}^{k-1/2} = \frac{1}{2}\Delta t^k \sum_{I=1}^{8} \left[N_{Ip,j}^k \tilde{v}_{iI}^{s,k-1/2} + N_{Ip,i}^k \tilde{v}_{jI}^{s,k-1/2} \right], \tag{56}$$

$$\Omega_{ijp}^{k-1/2} = \frac{1}{2} \sum_{I=1}^{8} \left[N_{Ip,j}^k \tilde{v}_{iI}^{s,k-1/2} - N_{Ip,i}^k \tilde{v}_{jI}^{s,k-1/2} \right] \tag{57}$$

Loop over all the elements to calculate their incremental strains and spin tensors based on the adjusted velocities $\tilde{v}_{iI}^{r,k-1/2}$ by using Eqs. (56) and (57), respectively.

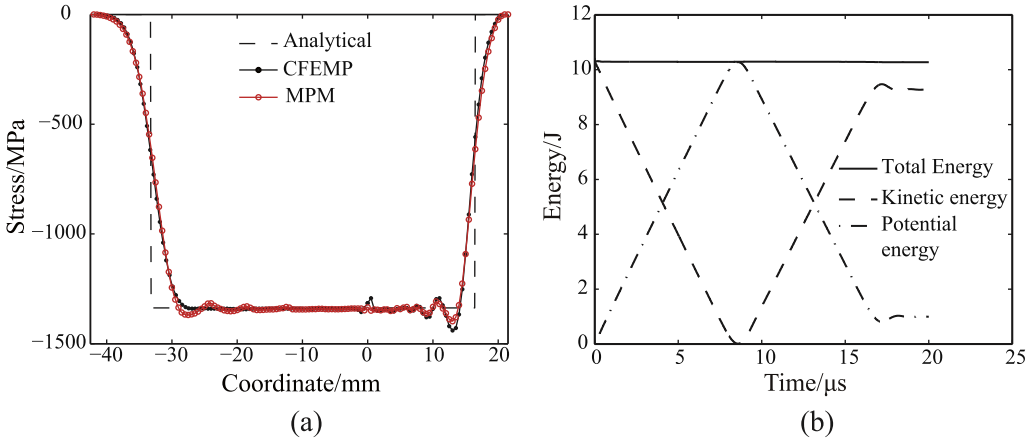

Fig. 8. (a) Plate impact stress profile at time 6.8 μs; (b) Energy evolution of plate impact.

Then update the stresses of particles and elements by corresponding constitutive law and EOS. The density of a particle or an element is updated by

$$\rho_p^{k+1} = \rho_p^k / \left(1 + \Delta\varepsilon_{iip}^{k-1/2}\right). \tag{58}$$

6. Calculate the nodal force.
   Loop over all the particles to calculate internal forces $f_{il}^{\text{int},k}$ and external forces $f_{il}^{\text{ext},k}$ of grid points by using Eqs. (13) and (14), respectively.
   Loop over all the elements to calculate the nodal internal forces $f_{il}^{\text{int},k}$, external forces $f_{il}^{\text{ext},k}$ and hourglass resisting forces $f_{il}^{\Gamma,k}$. If the node I is fixed in i direction, set $f_{il}^k = f_{il}^{\text{ext},k} + f_{il}^{\text{int},k} + f_{il}^{\Gamma,k} = 0$ to make its acceleration $a_{il}^k = 0$. Then loop over all the hybrid nodes to map their nodal forces to grid points.
7. Loop over all contact points to calculate $f_{I,2}^{\text{nor},k}$, the second term of the normal contact forces, by Eq. (39) and the tangential contact force $f_I^{\text{tan},k}$ by Eq. (44).
8. Loop over all the grid points to update their momenta by

$$p_{il}^{g,k+1/2} = \tilde{p}_{il}^{g,k-1/2} + \Delta t^k \left(f_{il}^{g,k} + f_{I,2}^{\text{nor},k} n_{il}^{g,k} + f_I^{\text{tan},k} t_{il}^{g,k}\right) \tag{59}$$

   and apply the boundary conditions of the background grid.
9. Loop over all the particles to update their velocities and positions by using

$$v_{ip}^{k+1/2} = v_{ip}^{k-1/2} + \Delta t^k \sum_{I=1}^{n_g} \left(f_{il}^{g,k} + (f_{I,1}^{\text{nor},k} + f_{I,2}^{\text{nor},k}) n_{il}^{g,k} + f_I^{\text{tan},k} t_{il}^{g,k}\right) N_{Ip}^k / m_I^k \tag{60}$$

   and Eq. (24), respectively.
10. Loop over all the FE nodes to update their velocities and positions by Eqs. (26) and (27), respectively. Loop over all the hybrid nodes to update their velocities and positions by Eqs. (25) and (27), respectively, and label them as FE nodes.
11. Discard the deformed background grid and define a new regular background grid. Return to step 1 to start a new time step.

Table 2
Information for plate impact.

	Elements	Particles	Time steps to 20 μs	Cost/s	Separation time/μs
Analytical	–	–	–	–	17.28
CFEMP	3024	12,096	2756	212	17.3
MPM	–	36,288	2777	582	17.3

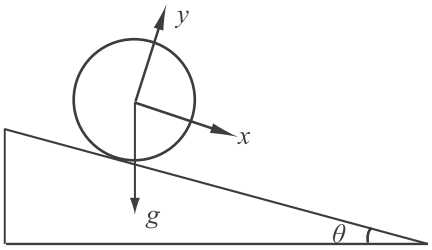

Fig. 9. A sphere rolling on an inclined plate.

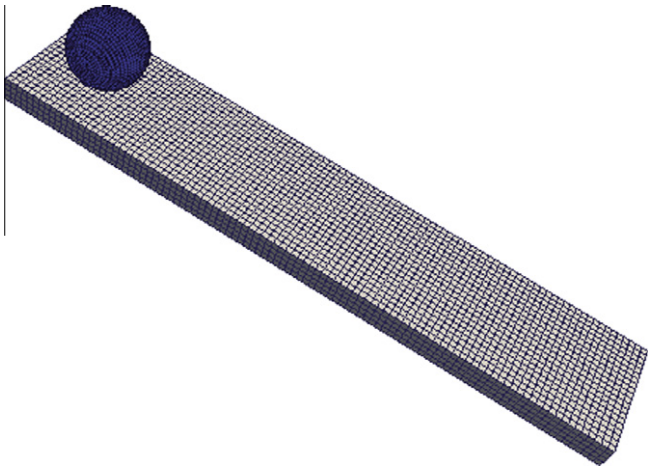

Fig. 10. Typical discretization of a sphere rolling on an inclined plate.

5. Numerical examples

5.1. Symmetric plate impact

A series of plate impact with different material laws applied are investigated here to validate the accuracy and efficiency of CFEMP. In all the simulations, the initial gap between the two plates is set to zero, and the friction coefficient is zero.

The first example is a symmetric plate impact. The length of the plate is 21 mm and the area is 3 × 3 mm. Two plates are traveling with an equal and opposite velocity of 100 m/s towards each other. Elastic material law is applied for both plates, whose Young's modulus $E = 65 \times 10^3$ MPa, Poisson's ratio $\nu = 0$, and density $\rho = 2.75 \times 10^{-3}$ g/mm^3. A typical discretization of the two plates is shown in

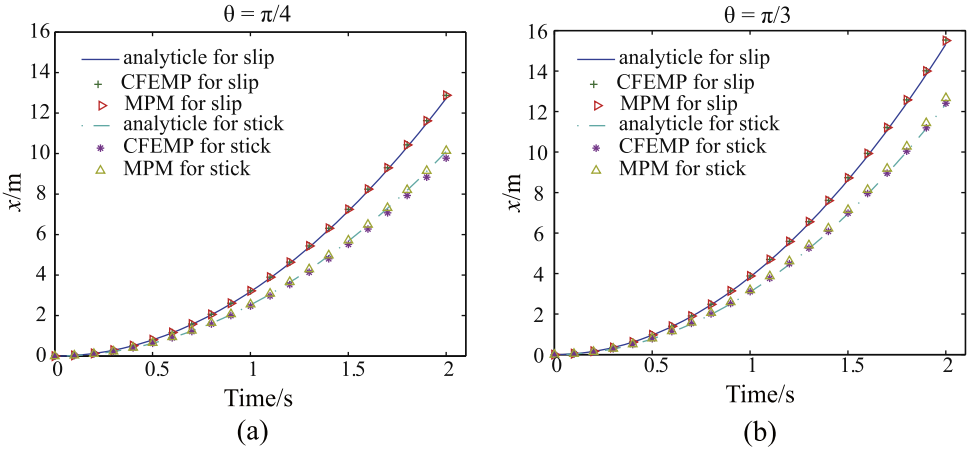

Fig. 11. Center-of-mass position for sphere as a function of time: (a) the angle of inclination $\theta = \pi/4$, and coefficient of friction $\mu = 0.1$ and 0.4, respectively. (b) the angle of inclination $\theta = \pi/3$, and coefficient of friction $\mu = 0.2$ and 0.6, respectively.

Table 3
Simulation cost for sphere rolling on the inclined plate.

	Elements	Particles	Time steps to 2.0 ms	Cost/s
CFEMP	8000	17,259	3391	144
MPM	–	81,259	3622	456

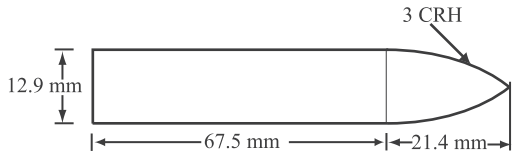

Fig. 13. Schematic of the ogive-nose projectile.

Fig. 4, where the left plate is modeled by FEM, while the right plate by MPM. Plane strain assumption is applied along the sides of the model, which result in a 1D wave propagation in the plates. The element size is 0.5 mm, the grid cell size 0.5 mm, and the particle space 0.25 mm.

The numerical results of stress profile and separation time are in good agreement with 1D analytical solution. Fig. 5(a) compares the stress profiles in the plates for time 3.0 μs obtained by CFEMP and 1D analytical solution, while Fig. 5(b) shows the energy curve of the simulation. The protuberance of the profile given by CFEMP is located in the region of MPM near to the contact interface due to the asymmetry of discrete of MPM and FEM, but the influence is limited to local region so that it could be ignored. Moreover, some oscillations are observed in the MPM domain but not in the FEM domain. Table 1 lists the separation time of two plates and the computational cost for both CFEMP and MPM, which shows that the CFEMP is more efficient than the MPM for this simulation.

Obviously, the accuracy of the contact method is dependent on the ratio R between the finite element size and MPM cell size. Therefore, the aspect ratio effect is further investigated for the example given above by fixing the cell size of 0.5 mm and increasing the finite element size from 0.25 mm to 1.5 mm. The numerical results obtained for different R are illustrated in Fig. 6, which shows that the numerical result agrees well with the analytical result when the R is less than 2, but significant oscillation can be seen when the R is larger than 2 in the profile of MPM domain due to the unmatched mesh at the contact interface. Besides, penetration is observed in the simulation due to the unmatched mesh for R larger than 1.

In addition, an elasto-plastic material law with isotropic hardening is applied for both plates, whose Young's modulus $E = 65 \times 10^3$ MPa, tangent modulus $E_T = 30 \times 10^3$ MPa, Yield stress $\sigma_y = 300$ MPa and density $\rho = 2.75 \times 10^{-3}$ g/mm^3. Other parameters are the same to the above example and set $R = 1$. In this example, double waves of elastic wave and plastic wave will propagate along the plates at the same time. The numerical result is given in

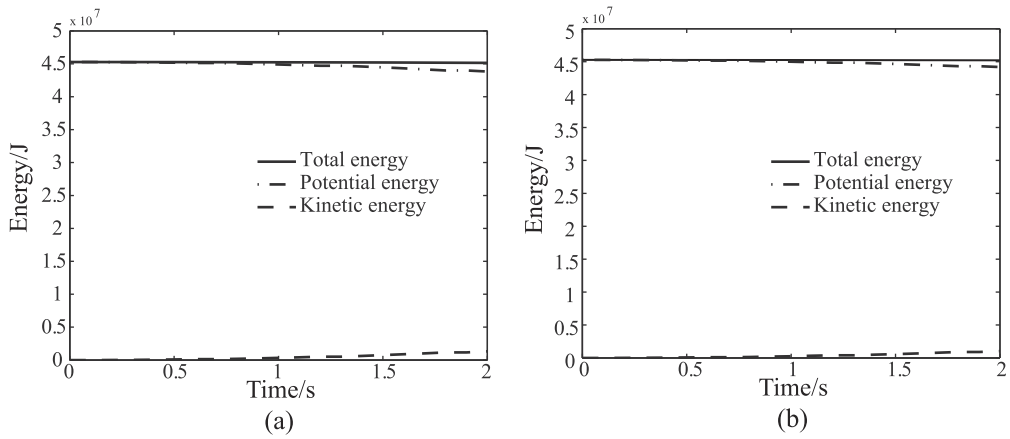

Fig. 12. Energy evolution of sphere rolling: (a) for case 1; (b) for case 2.

Table 4
Material constants of projectile.

ρ (g/mm^3)	E (GPa)	μ	σ_y (GPa)	E_T (GPa)
0.00785	202	0.3	1.43	14.759

Table 5
Material constants of A6061-T651 for strength model and EOS.

ρ (g/mm^3)	E (GPa)	μ	A (MPa)	B (MPa)	n	C	m
0.0027	69	0.3	262	52.1	0.41	0	0.859
c_0 (mm/ms)	s	γ_0	T_{melt} (K)	T_{room} (K)			
5,350	1.34	2.0	875	293			

Table 6
Effect of grid cell size and element size on the simulation results.

Case	Cell size (mm)	Number of particles for target	Number of elements for projectile	Residual velocity (m/s)
1	3	90,593	5440	286
2	2	314,600	18,144	418
3	1.5	756,315	42,752	433
4	1	2,516,800	145,152	456
Experiments	–	–	–	455

Fig. 7, which shows that the numerical result is close to the 1D analytical solution.

5.2. Asymmetric elastic plate impact

An asymmetric elastic plate impact with different length and material parameters is further studied here. One plate is with size of $3 \times 3 \times 42$ mm and modeled by elastic constitutive with $E = 65 \times 10^3$ MPa, $\rho = 2.75 \times 10^{-3}$ g/mm^3, while the other is with size of $3 \times 3 \times 21$ mm and modeled by elastic constitutive with $E = 32.5 \times 10^3$ MPa, $\rho = 5.5 \times 10^{-3}$ g/mm^3. Other parameters are the same to example in Section 5.1 and set $R = 1$. The sound speed of the first plate is two times that of the other, but the impedance is matched. The longer plate is modeled by FEM, while the other by MPM.

Fig. 8(a) compares the stress profile obtained by CFEMP and MPM with the analytical solution at time 3.6 μs. The energy curve is shown in Fig. 8(b). Table 2 lists the information about the contact separation time and computational cost, which shows the accuracy and efficiency of CFEMP method is higher than that of MPM.

5.3. Sphere rolling simulation

The third example is an elastic sphere rolling on an inclined elastic plate due to gravity, as shown in Fig. 9. The plate is inclined at an angle θ from the horizontal. The radius of sphere is $R = 1.6$ m, and the size of plate is $20 \times 4 \times 0.8$ m. The gravity $g = 10$ g/s^2 is vertically downward.

From rigid body dynamics, the sphere will roll and either stick or slip at the point of contact depending on the angle of inclination and the friction coefficient. For convenience, the direction tangent to the surface of the plane is chosen as x-direction, so that the kinematics equation of the center-of-mass of the sphere can be expressed as

$$x(t) = \begin{cases} x_0 + \frac{1}{2}gt^2(\sin\theta - \mu\cos\theta) & \tan\theta > 3\mu \quad \text{(roll and slip)}, \\ x_0 + \frac{5}{14}gt^2\sin\theta & \tan\theta \leqslant 3\mu \quad \text{(pure rolling)}, \end{cases}$$

where $x_0 = 0$ is the x-component of the initial center-of-mass position.

In the simulation, the sphere has a Young's modulus of $E = 4.2 \times 10^6$ Pa, Poisson's ratio of $\nu = 0.4$, and density of $\rho = 1000$ Kg/m^3. The plate has a Young's modulus of $E = 4.2 \times 10^7$ Pa, Poisson's ratio of $\nu = 0.4$, and density of $\rho = 10{,}000$ Kg/m^3. As shown in Fig. 10, the plate is modeled by FEM with fixed boundary condition at the bottom surface, while the sphere is modeled by MPM. The element size is 0.2 m, cell size is 0.2 m, and particle space is 0.1 m.

Four cases are studied. In the first and the second cases, the inclined angle is $\theta = \pi/4$ with frictional coefficient of $\mu = 0.1$ and 0.4, respectively. In the third and fourth cases, the inclined angle is $\theta = \pi/3$ with frictional coefficient of $\mu = 0.2$ and 0.6, respectively. In the first and third cases, the sphere will roll and slip, in other cases the sphere will roll and stick.

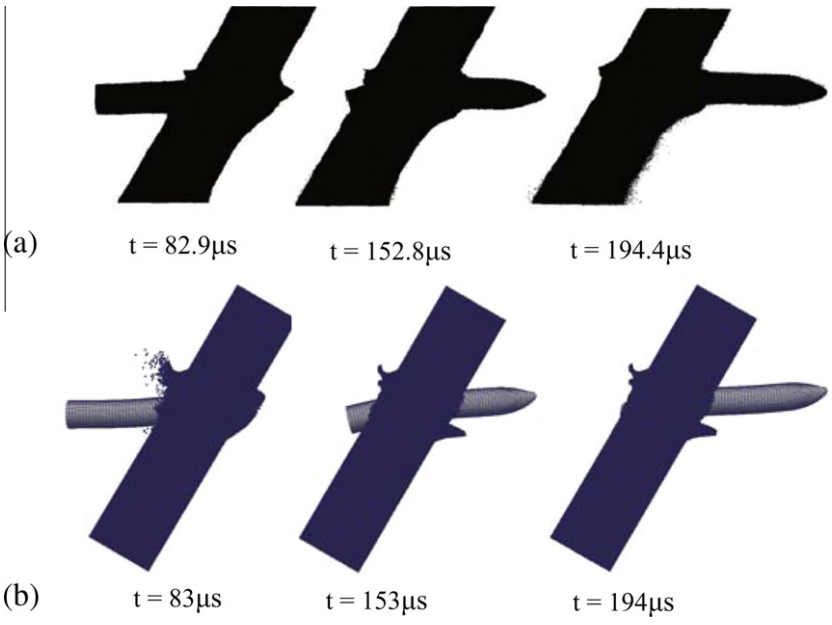

Fig. 14. Projectile-target interaction at the striking velocity $v_0 = 575$ m/s.

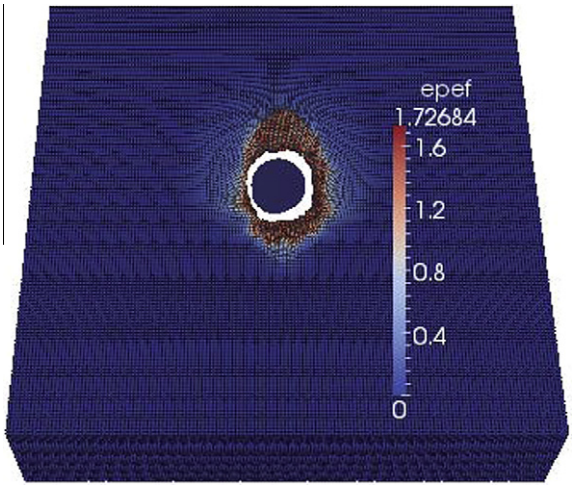

Fig. 15. Contour plot of the effective plastic strain at final time 0.28 μs.

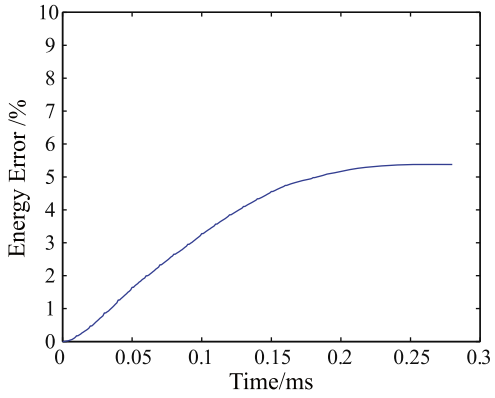

Fig. 16. The energy error for the case 4 in time.

Fig. 11(a) compares the numerical results of the center-of-mass position with the analytical solutions for case 1 and 2, and Fig. 11(b) for case 3 and 4. The numerical results obtained by CFEMP method are in good agreement with analytical results. Table 3 lists the computational cost of case 1 for both CFEMP and MPM, which shows that the CPU time required for the MPM simulation is more than that of CFEMP simulation. The energy curves of case 1 and 2 are illustrated in Fig. 12.

5.4. Perforation of thick plate

In order to validate the robustness of CFEMP method, a projectile against oblique thick plate is investigated. The inclined angle is 30°. The experiments were conducted by Piekutowski et al. [48], where ogive-nose hardened steel projectiles and 6061-T651 aluminum plates were adopted. As shown in Fig. 13, the projectile has a length of 88.9 mm and a diameter of 12.9 mm with a 3.0 caliber-radius-head. The target has a thickness of 26.3 mm and an area of 110×110 mm.

Table 7
The projectile's residual velocities for different striking velocities (m/s).

v_0	Experiment	CFEMP	MPM
400	217	229	241
446	288	293	306
575	455	456	471
730	655	631	652

The projectile is discretized with an unstructured elements arrangement and modeled by an elasto-plastic material law with isotropic hardening. The target is discretized with a structured particle arrangement and modeled by an elastic–plastic material law, Johnson–Cook model whose yield stress is calculated by

$$\sigma_y = \left(A + B\bar{\varepsilon}_p^n\right)(1 + C\ln\dot{\varepsilon}^*)(1 - T^{*m}),$$

where A, B, C, n and m are the material constants, $\bar{\varepsilon}_p$ is the effective plastic strain, $\dot{\varepsilon}^* = \dot{\bar{\varepsilon}}^p/\dot{\varepsilon}_0$ is the dimensionless plastic strain rate for $\dot{\varepsilon}_0 = 1.0\ \mathrm{s}^{-1}$, and $T^* = (T - T_{\mathrm{room}})/(T_{\mathrm{melt}} - T_{\mathrm{room}}) \in [0,1]$ is the dimensionless temperature. Besides, the pressure of target material is updated by the Mie–Gruneisen EOS. Material failure is taken into account by setting the deviatoric components of the stress tensor to zero when the effective plastic strain reaches the plastic strain

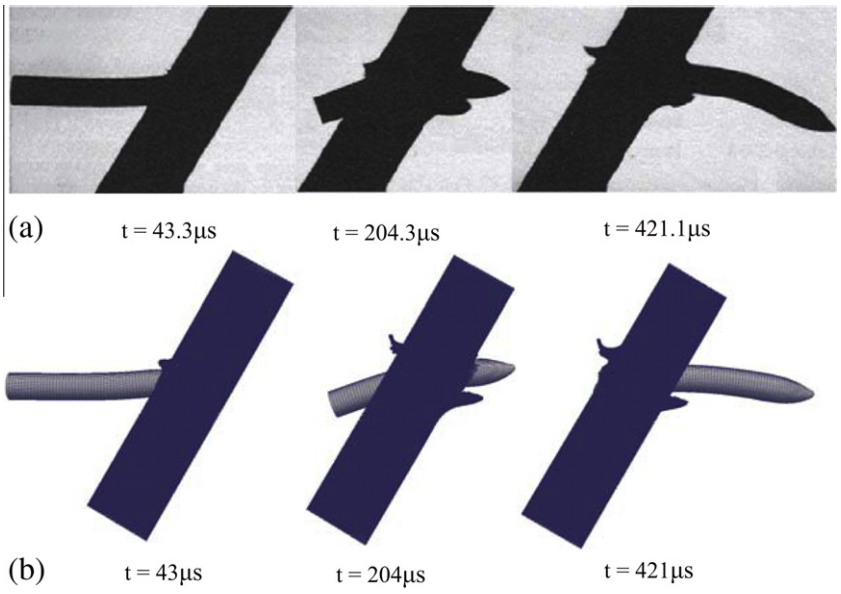

Fig. 17. Projectile-target interaction at the striking velocity $v_0 = 400$ m/s.

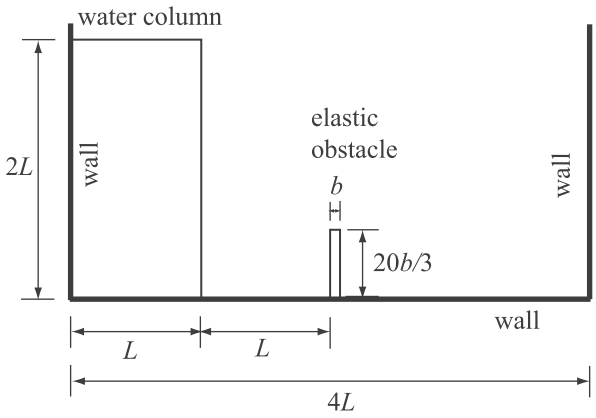

Fig. 18. Schematic of the water column with an elastic obstacle.

Table 8
Material constants of water.

ρ (kg/m^3)	c_0 (m/s)	s	γ_0
1000	1647	1.921	0.1

ε_{fail} = 1.6 at failure. The material constants for the projectile and the target listed in Tables 4 and 5, respectively, are taken from references [48,49]. In our simulation, the friction between projectile and target is ignored.

We will focus first on the experiment of projectile with striking velocity of 575 m/s. Four different cases are investigated to study the mesh refinement effect on the accuracy of CFEMP as shown in Table 6. In each case, the particle space is half of the cell size and the ratio R ranges from 0.14 to 1 due to the complicated geometrical shape of ogive-nose. The residual velocity of the projectile given by CFEMP is listed in Table 6, which shows that the numerical results converge to the experimental data with decreasing the sizes of the cell and the element.

In case 4, the residual velocity of the projectile obtained by CFEMP method is 456 m/s, which is closed to experimental result. Moreover, the projectile-target interactions obtained in the experiment and in the simulation are compared in Fig. 14, where Fig. 14(a) shows a sequence of X-ray photographs at three times of impact and Fig. 14(b) shows the numerical results at the same times. The projectile's shapes obtained by the CFEMP method are consistent with the experimental results during the perforation process. In addition, the effective plastic strain contour plot of the target at 0.28 ms is shown in Fig. 15, and the energy error in time for case 4 is illustrated in Fig. 16 which does not exceed 5.5%.

Furthermore, the projectile with different striking velocity v_0 is investigated with the same cell and element sizes used in case 4. The residual velocity of projectile given by both CFEMP and MPM is listed in Table 7, which shows that the numerical results are close to the experimental data. The residual velocities given by CFEMP method are less than that of MPM, but the difference is not significant. The computational cost of CFEMP is more than that of MPM due to the smallest ratio R is less than 1, but the efficiency of CFEMP per time step is higher than that of MPM.

From the observation of experiments, the shapes of the projectiles are dependent on the striking velocity v_0. Therefore, the projectile-target interaction for projectile with v_0 = 400 m/s is given in Fig. 17. From the comparison, we can find that the projectile's

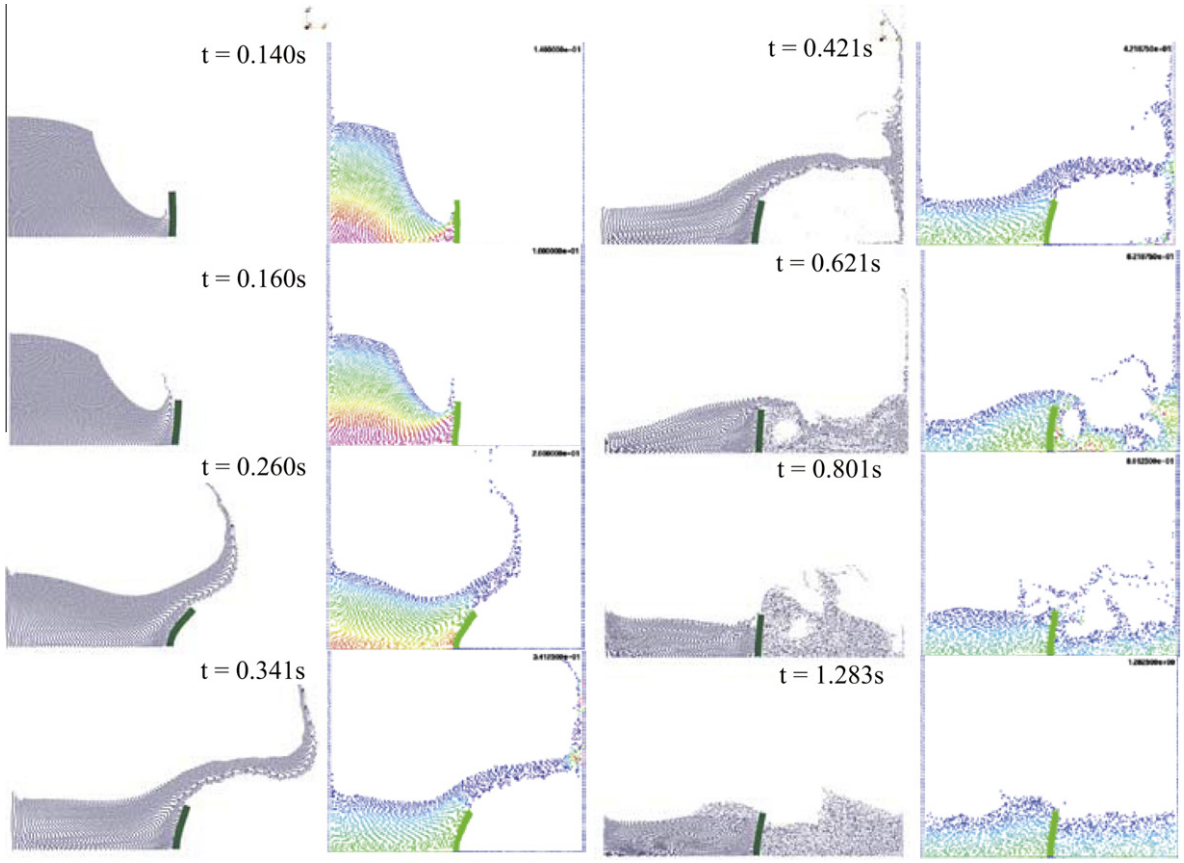

Fig. 19. Comparison between CFEMP results and PFEM [50] results for water column collapse on a flexible obstacle.

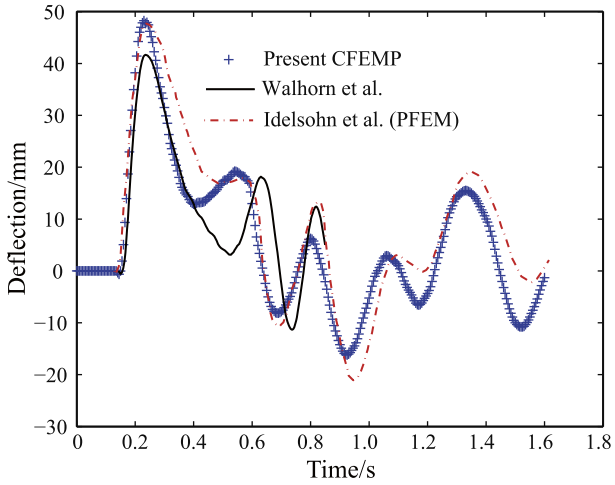

Fig. 20. Comparison between numerical results for time history of the displacement of the upper left corner of the obstacle.

shapes and the ballistic trajectory obtained by CFEMP method are consistent with the experimental data during the perforation process.

5.5. Water column collapse simulation

Finally, a fluid–structure interaction problem is investigated by CFEMP. As shown in Fig. 18, a water column will collapse through a flexible obstacle to the right wall due to the gravity.

The water column is of width $L = 146$ mm and of height $2L$, and the flexible obstacle is of width $b = 12$ mm and of height 80 mm. The gap between obstacle and water column is of length L. The water will flow freely due to the gravity acting downwards with $g = 9.8 \times 10^{-3}$ mm/ms^2. The air is neglected. In the simulation, the flexible obstacle is modeled by FEM with density $\rho = 2.5 \times 10^{-3}$ g/mm^3, Young modulus $E = 1$ MPa and Poisson ratio $v = 0$. The water column is modeled by MPM with null material model and Mie–Gruneisen EOS, whose material constants are listed in Table 8. In order to keep the surface of water smoothed, the water is assumed to be able to sustain certain level of tension, which is set to 0.006 MPa. Plane strain assumption is applied in the simulation. The particle space is 2 mm, and both the cell and the element sizes are 4 mm, where $R = 1$. Structured discretization is used for both water and obstacle, which consist of 10,608 particles for water, and 60 elements for the obstacle.

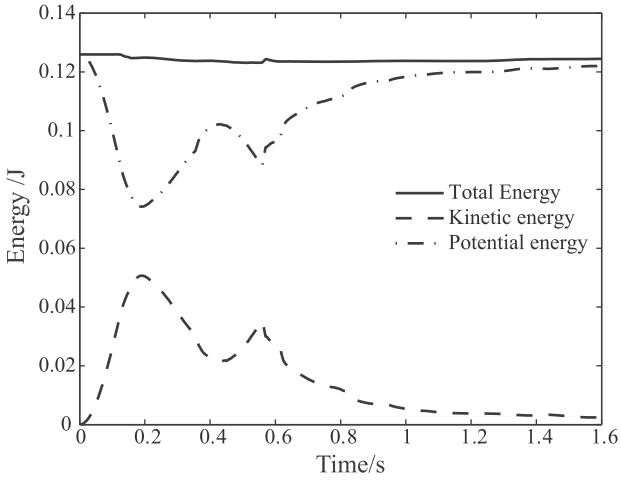

Fig. 21. Energy evolution of collapse of water column.

Although there are no available experimental results, this problem was investigated by other researchers using PFEM [50] and a staggered method with level-set method [51], respectively. Here, the numerical results of CFEMP method are compared with the results given by Idelsohn et al. [50], as shown in Fig. 19. Both the deformed shape of the obstacle and the free surface of water obtained by CFEMP agree well with those obtained by PFEM. The time history of the deflection of the upper left corner of the obstacle is compared with other available numerical results [50,51] in Fig. 20. Finally, the energy curve of this problem is given in Fig. 21.

6. Conclusion

In this paper, we put forward a contact method to handle the interaction between the body modeled by FEM and the body modeled by MPM. In this method, the FE nodes located on the contact interface are treated as hybrid nodes, whose momentum equations are established and integrated on the contact grid points like particles. The contact force is calculated on the background grid points and imposed on the hybrid nodes and particles. Different from the contact of MPM, the normal vector of body surface is calculated by the surface of elements for FEM body.

Based on the contact method, a coupled finite element–material point method is proposed in this paper, in which the body with mild deformation is modeled by FEM, while the body with extreme deformation is modeled by MPM. The accuracy of FEM is higher than MPM for body with mild deformation because the particle quadrature rather than Gauss quadrature is used in MPM. Besides, the ratio between element size and grid cell size should be less than 2 to avoid penetration occurring due to the background grid based contact method. Central difference time integration is used to integrate the momentum equation so that if the critical time step is controlled by the MPM body the efficient of CFEMP is higher than that of MPM. Two plates impact and a sphere rolling on an inclined plate are investigated to validate the accuracy and efficiency of CFEMP, and a series of impact experiment of projectile against an inclined plate are studied to validate the robustness of CFEMP. Finally, a fluid–structure interaction of collapse of water column through an elastic obstacle is studied. All the problems are three dimensional and the numerical results obtained by CFEMP are in good agreement with analytical solution or results available in the literature.

References

[1] P.W. Randles, L.D. Libersky, Smoothed particle hydrodynamics: some recent improvements and applications, Comput. Methods Appl. Mech. Engrg. 139 (1996) 375–408.
[2] L. Libersky, A.G. Petschek, T.C. Carney, et al., High strain Lagrangian hydrodynamics a three-dimensional SPH code for dynamics material response, J. Comput. Phys. 109 (1993) 67–75.
[3] R. Stellingwerf, C. Wingate, Impact modeling with smooth particle hydrodynamics, Int. J. Impact Engrg. 14 (1993) 707–718.
[4] G.R. Johnson, R.A. Stryk, S.R. Beissel, SPH for high velocity impact computations, Comput. Methods Appl. Mech. Engrg. 139 (1–4) (1996) 347–373.
[5] G.R. Johnson, S.R. Beissel, Normalized smoothing functions for SPH impact computations, Int. J. Numer. Methods Engrg. 39 (16) (1996) 2725–2741.
[6] T. Rabczuk, J. Eibl, Modeling dynamic failure of concrete with meshfree methods, Int. J. Impact Engrg. 32 (2006) 1878–1897.
[7] M.B. Liu, G.R. Liu, Z. Zong, K.Y. Lam, Computer simulation of high explosive explosion using smoothed particle hydrodynamics methodology, Computers & Fluids 32 (3) (2003) 305–322.
[8] M.B. Liu, G.R. Liu, K.Y. Lam, Z. Zong, Meshfree particle simulation of the detonation process for high explosives in shaped charge unlined cavity configurations, Shock Waves 12 (2003) 509–520.
[9] T. Belytschko, M. Tabbara, Dynamic fracture using element-free Galerkin methods, Int. J. Numer. Methods Engrg. 39 (6) (1996) 923–938.
[10] T. Rabczuk, T. Belytschko, Cracking particles: a simplified meshfree method for arbitrary evolving cracks, Int. J. Numer. Methods Engrg. 61 (2004) 2316–2343.
[11] T. Rabczuk, T. Belytschko, A three-dimensional large deformation meshless method for arbitrary evolving cracks, Comput. Methods Appl. Mech. Engrg. 196 (2007) 2777–2799.

[12] T. Rabczuk, G.S. Zi, A meshfree method based on the local partition of unity for cohesive cracks, Comput. Mech. 39 (6) (2007) 743–760.
[13] T. Rabczuk, S. Bordas, G.S. Zi, A three-dimensional meshfree method for continuous multiple-crack initiation, propagation and junction in statics and dynamics, Comput. Mech. 40 (3) (2007) 473–495.
[14] S.R. Idelsohn, E. Onate, F. Del Pin, The particle finite element method: a powerful tool to solve incompressible flows with free-surfaces and breaking waves, Int. J. Numer. Methods Engrg. 61 (7) (2004) 964–989.
[15] T. Rabczuk, R. Gracie, J.H. Song, T. Belytschko, Immersed particle method for fluid-structure interaction, Int. J. Numer. Methods Engrg. 81 (2010) 48–71.
[16] D. Sulsky, Z. Chen, H.L. Schreyer, A particle method for history-dependent materials, Comput. Methods Appl. Mech. Engrg. 118 (1–2) (1994) 179–196.
[17] D. Sulsky, H.L. Schreyer, Axisymmetric form of the material point method with applications to upsetting and taylor impact problems, Comput. Methods Appl. Mech. Engrg. 139 (1–4) (1996) 409–429.
[18] L.M. Shen, A rate-dependent damage/decohesion model for simulating glass fragmentation under impact using the material point method, Comput. Model. Engrg. Sci. 49 (1) (2009) 23–45.
[19] X. Zhang, K.Y. Sze, S. Ma, An explicit material point finite element method for hyper-velocity impact, Int. J. Numer. Methods Engrg. 66 (4) (2006) 689–706.
[20] Y.P. Lian, X. Zhang, X. Zhou, Z.T. Ma, A FEMP method and its application in modeling dynamic response of reinforced concrete subjected to impact loading, Comput. Methods Appl. Mech. Engrg. 200 (2011) 1659–1670.
[21] W.Q. Hu, Z. Chen, Model-based simulation of the synergistic effects of blast and fragmentation on a concrete wall using the MPM, Int. J. Impact Engrg. 32 (12) (2006) 2066–2096.
[22] J.E. Guillkey, T.B. Harman, B. Banerjee, An Eulerian–Lagrangian approach for simulating explosions of energetic devices, Comput. Struct. 85 (2007) 660–674.
[23] Y.J. Guo, J.A. Nairn, Three-dimensional dynamic fracture analysis using the material point method, Comput. Model. Engrg. Sci. 16 (3) (2006) 141–155.
[24] J. Ma, H.B. Lu, R. Komanduri, Structured mesh refinement in generalized interpolation material point (GIMP) method for simulation of dynamic problems, Comput. Model. Engrg. Sci. 12 (3) (2006) 213–227.
[25] L.M. Shen, Z. Chen, A silent boundary scheme with the material point method for dynamic analyses, Comput. Model. Engrg. Sci. 7 (3) (2005) 305–320.
[26] A.R. York II, D. Sulsky, H.L. Schreyer, Fluid-membrane interaction based on the material point method, Int. J. Numer. Methods Engrg. 48 (2000) 901–924.
[27] G. Anvar, A. Sumanta, A hybrid immersed boundary and material point method for simulating 3D fluid-structure interaction problems, Int. J. Numer. Methods Fl. 56 (2008) 2151–2177.
[28] H.W. Zhang, K.P. Wang, Z. Chen, Material point method for dynamic analysis of saturated porous media under external contact/impact of solid bodies, Comput. Methods Appl. Mech. Engrg. 198 (2009) 1456–1472.
[29] T. Rabczuk, S.P. Xiao, M. Sauer, Coupling of mesh-free methods with finite elements: basic concepts and test results, Commun. Numer. Methods Engng. 22 (2006) 1031–1065.
[30] S.W. Attaway, M.W. Heinstein, J.W. Swegle, Coupling of smooth particle hydrodynamics with the finite element method, Nucl. Engrg. Des. 150 (1994) 199–205.
[31] G.R. Johnson, Linking of Lagrangian particle methods to standard finite element methods for high velocity impact computations, Nucl. Engrg. Des. 150 (1994) 265–274.
[32] T. Belytschko, D. Organ, Y. Krongauz, A coupled finite element – element – free Galerkin method, Comput. Mech. 17 (1995) 186–195.
[33] D. Hege, Element-free Galerkin methods in combination with finite element approaches, Comput. Methods Appl. Mech. Engrg. 135 (1996) 143–166.
[34] T. Rabczuk, T. Belytschko, Application of mesh free methods to static fracture of reinforced concrete structures, Int. J. Fract. 137 (2006) 19–49.
[35] S. Attaway, M. Heinstein, J. Swegle, Coupling of smooth particle hydrodynamics with the finite element method, Nucl. Engrg. Des. 150 (1994) 199–205.
[36] G.R. Johnson, R.A. Stryk, Conversion of 3D distorted element method for hypervelocity impact simulation, Int. J. Impact Engrg. 28 (2003) 947–966.
[37] T.D. Vuyst, R. Vignjevic, J.C. Campbell, Coupling between meshless and finite element methods, Int. J. Impact Engrg. 31 (2005) 1054–1064.
[38] W.K. Liu, R.A. Uras, Y. Chen, Enrichment of the finite element method with reproducing kernel particle method, J. Appl. Mech. 135 (1997) 143–166.
[39] W.K. Liu, W. Han, H.S. Lu, S.F. Li, J. Cao, Reproducing kernel element method. Part I: Theoretical formulation, Comput. Methods Appl. Mech. Engrg. 193 (12–14) (2004) 933–951.
[40] S.F. Li, H.S. Lu, W. M Han, W.K. Liu, D.C. Simkins, Reproducing kernel element method Part II: Globally conforming I^m/C^n hierarchies, Comput. Methods Appl. Mech. Engrg. 193 (12–14) (2004) 953–987.
[41] D.C. Simkins Jr., S. F Li, H. S Lu, W.K. Liu, Reproducing kernel element method. Part IV: Globally compatible C^n ($n \geqslant 1$) triangular hierarchy, Comput. Methods Appl. Mech. Engrg. 193 (2004) 1013–1034.
[42] S.G. Bardenhagen, J.U. Brackbill, D. Sulsky, The material-point method for granular materials, Comput. Methods Appl. Mech. Engrg. 187 (3–4) (2000) 529–541.
[43] P. Huang, X. Zhang, S. Ma, X. Huang, Contact algorithms for the material point method in impact and penetration simulation, Int. J. Numer. Methods Engrg. 85 (4) (2011) 498–517.
[44] W. Hu, Z. Chen, A multi-mesh mpm for simulating the meshing process of spur gears, Comput. Struct. 81 (2003) 1991–2002.
[45] J.O. Hallquist, LS-DYNA Theoretical Manual, Livermore Software Technology Corporation, 1998.
[46] D.P. Flanagan, T. Belytschko, A uniform strain hexahedron and quadrilateral with orthogonal hourglass control, Int. J. Numer. Methods Engrg. 17 (1981) 679–706.
[47] Z. Ma, X. Zhang, P. Huang, An object-oriented mpm framework for simulation of large deformation and contact of numerous grains, Comput. Model. Engrg. Sci. 55 (1) (2010) 61–87.
[48] A.J. Piekutowski, M.J. Forrestal, K.L. Poormon, T.L. Warren, Peroration of aluminum plates with ogive-nose steel rods at normal and oblique impacts, Int. J. Impact Engrg. 18 (1996) 877–887.
[49] M.A. Meyers, Dynamic Behavior of Materials, John Wiley & Sons, 1994.
[50] S.R. Idelsohn, J. Marti, A. Limache, E. O?ate, Unified Lagrangian formulation for elastic solids and incompressible fluids: application to fluid-structure interaction problems via the PFEM, Comput. Methods Appl. Mech. Engrg. 197 (19–20) (2008) 1762–1776.
[51] E. Walhorn, A. Kolke, B. Hubner, D. Dinkler, Fluid-structure coupling within a monolithic model involving free surface flows, Comput. Struct. 83 (2005) 2100–2111.